Journal of Materials Processing Technology (2014). 214(2), 436-444.
DOI: http://dx.doi.org/10.1016/j.jmatprotec.2013.09.014

Water soluble Invar 36 feedstock development for μPIM

J. Hidalgo [a,*], A. Jiménez-Morales [a], T. Barriere [b], J.C. Gelin [b], J.M. Torralba [a,c]

[a] *Materials Science Department at Carlos III University of Madrid, Leganés, Spain*
[b] *Applied Mechanics Department at FEMTO-ST Institute, Besanç on, France*
[c] *IMDEA Materials Institute, Getafe, Spain*

* Corresponding author at: Avd. Universidad 30, 28911 Leganés, Spain.
Tel.: +34 916249482. *E-mail address:* jhidalgo@ing.uc3m.es (J. Hidalgo).

Abstract: A water soluble binder system based on cellulose acetate butyrate (CAB) and polyethylene glycol (PEG) is proposed and investigated to carry out a micro powder injection moulding (μPIM) process with an Invar 36 alloy powders. The overall process was optimised with an emphasis on the determination of the optimal solid loading. Several methodologies were evaluated and compared to determine this parameter. A full μ PIM was performed with different powder content feedstocks. Dog bone-type micro test parts were fabricated thereof and their mechanical properties were evaluated. Solid loadings up to 65 vol.%resulted to have the most equilibrated properties to successfully fabricate Invar 36 micro parts with the selected powder and binder system.

Keywords: Micro powder injection moulding, Invar 36, Solid loading optimisation

1. Introduction

Micro powder injection moulding (μPIM) is a leading manufacturing method for the production of complex, net-shaped and high performance micro components at competitive costs. As remarked by Heaney (2012) and many other authors, this promising technology has experienced rapid growth due to the rising demand for the application of micro components. Attia and Alcock (2011) compiled a thorough revision of μ PIM. Micro components are classified into the three categories, namely: micro parts, microstructured components and micro-precision parts. Micro-precision parts are employed for different application, includding micro moulds, micro-mechanics, micro-fluidics, micro-sensors, microscale medical devices and other micro systems. Ruh et al. (2012) performed studies regarding size accuracy of microgear wheels. They stated that this kind of parts require high dimensional stability and should have tolerances in the micron range. Dimensional changes with temperature can be minimised by employing materials with low coefficients of thermal expansion (CTE). In that respect, Maslyuk et al. (2003) reported that iron-nickel based Invar alloys are a potential alternative when an application demands simi-lar characteristics to austenitic stainless steel and also a thermal stability up to around 250 °C. Within the $Fe_x - Ni_{x-1}$ invar alloy family, Invar 36 (Fe_{64}–Ni_{36} according to DIN 1.3912) is a suitable material for precision components and utilities, such as clock-works, motor valves and physical or topographical devices. At a 0–100 °C temperature range, the CTE of the Fe_{64}–Ni_{36} invar is about (1–2) × 10^{-6} K^{-1}. Khomenko (2007) studied the origin and specific features of invar anomalies of physical properties of Fe-Ni alloys with FCC lattice. The low thermal expansion coefficient of the alloy is assumed to be due to the competition of magnetic and lattice contributions below the Curie temperature and is associated with the development of an austenitic FCC Fe–Ni lattice.

In μ PIM, a powder is mixed with a binder to obtain homogeneous feedstocks with features that allow for the injection of a part with the desired geometry. Once the part is moulded, the binder is removed and the powders are consolidated by sintering. Kong et al. (2012) employed different methodologies to the determina-tion of critical and optimal powder loadings for 316L fine stainless steel feedstocks for μ PIM. They concluded that the optimal powder content in the powder/binder feedstock and a suitable mixing tech-nique are the keys to achieve a homogeneous feedstock with the best properties after the injection, debinding and sintering steps. The literature includes several examples of the processing of low CTE invar type parts by PIM. Chi et al. (2011) performed PIM of com-plex invar alloy parts by combining Fe carbonyl and Ni carbonyl powders. do Nascimento et al. (2006) investigated different com-binations of Iron–Nickel–Cobalt invar type powders for developing PIM parts.

Fabrication of micro parts via μ PIM deals with issues that do not occur in conventional PIM processes. One important concern is the need of very fine powders with particle sizes in the micron range. This entail several problems. Suri et al. (2009) studied the influence of agglomerates in sinter parts. They concluded that to obtain a homogeneous and high quality feedstock for μ PIM, powder agglomeration in the feedstock should be avoided as it leads to defects in the final products. Particle sizes from 0.1 μm t o 1 5 μm

Table 1
Composition of the Invar 36 alloy with some characteristic particle size parameters.

Composition	Ni	Mn	Si	C	Fe	Particle size distribution	d_{10}	d_{50}	d_{90}
(mass%)	36.50	0.20	0.02	0.01	Balance	(μm)	1.9	3.4	5.9

are typically affected by agglomeration in PIM. Rajabi et al. (2012) reviewed works that use nanosized powder particles in PIM. Very fine particles and thus agglomeration-prone particles complicate the mixing and rheological behaviour of the as-prepared feedstocks. The micron size of the parts and the reduced diameters of the runners require a better flow behaviour than in conventional PIM. However, one benefit of small powders may be the decrease in the CTE with decreasing grain size. Bitkulov et al. (2006) reported a decrease in the CTE by a factor of two between an Invar 36 alloy with coarse and other with very fine grain sizes.

Another important issue to consider is the possible contamination with carbon and oxygen during the processing of micro-scale parts. Maslyuk et al. (2003) reviewed different Fe–Ni powder compositions physical properties and their applications and Nadutov et al. (2006) and Nadutov et al. (2009) investigated the mag-netic properties Fe–Ni–C invar alloys. Both works remarked that presence of C and other elements like N worsen the thermal stability of invar alloys. Hatate et al. (1990) reported that the CTE is directly affected by the concentration of carbon and nickel in Fe–(27∼40 wt.%) Ni Invar alloy. They also suggested that the CTE of the Fe–Ni–C Invar alloy is affected by Ni segregation in the primary austenite microstructure related to carbon content. How-ever, Wittenauer et al. (1994) and Wittenauer (1996) realised that small amounts of carbon could be beneficial to improve mechani-cal properties while an acceptable low CTE is maintained. Carbon presumably affects mechanical properties by strengthening the interstitial solid solution.

This work analyses various conventional methodologies along with other techniques to determine the optimal solid loading of Invar 36 low CTE alloy feedstocks for μ PIM. The microstructures and mechanical properties of as-produced parts were also investigated. A binder system based on cellulose acetate butyrate (CAB) and polyethylene glycol (PEG) was mixed with Invar 36 powders. The behaviour of this type of binder in PIM processes has received little study. Minseok et al. (2005) developed a binder system based on CAB, poly (methyl methacrylate) and PEG. In previous works of Bernardo et al. (2012) and Hidalgo et al. (2012) have presented CAB as an alternative to conventional polyolefins in binder formulations with water soluble PEG. In Hidalgo et al. (2013) this cellulose derivative polymeric substance has exhibited a better affinity with PEG than polyolefin compounds, which may lead to better feed-stock homogenisation. They realised that the selected CAB-based feedstocks also generally exhibit better rheological behaviour than

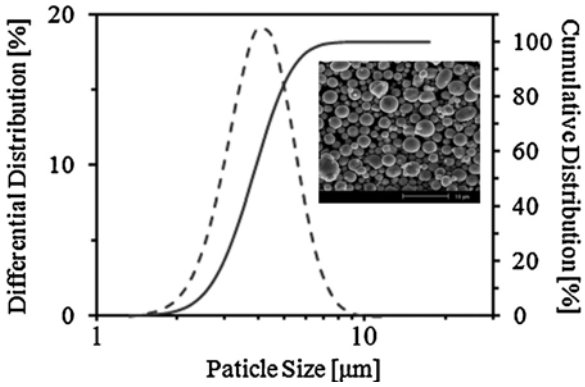

Fig. 1. Particle size distribution curves of the Invar 36 gas atomised powders together with an SEM image of the powder demonstrating the spherical particle shape.

polyolefin formulations. This commonly led on to higher optimal solid loadings, which was beneficial for improving the tolerance and properties of the final part. Nevertheless, CAB-based formulations have never been employed in PIM or μPIM of Invar 36 alloy. This study also demonstrates that this type of binder system is suitable for μPIM of an Invar 36 alloy up to 65 vol.%.

2. Experimental

Gas atomised Invar 36 alloy powders were used. The Invar 36 alloy consists of 36 wt% Ni, with the balance comprised of Fe except for some other trace elements. Table 1 presents the composition of the Invar 36 alloy. The powders were supplied by Sandvik Osprey Ltd. (UK). The powder has a particle size distribution with a d_{90} of 5.9 μm. Particle size distribution curves are presented in Fig. 1 along with a scanning electron microscopy (SEM) image showing the spherical shape of the particles.

The Invar 36 powders were mixed with a binder system based on a combination of several thermoplastic polymers, including differ-ent molecular weights of poly (ethylene glycol) (PEG) (supplied by Sigma–Aldrich) and two types of cellulose acetate butyrate (CAB)(supplied by Eastman) with a variable content of acetyl, butyryl and hydroxyl groups. The binder component contents and com-ponent specifications are included in Table 2.Several feedstocks

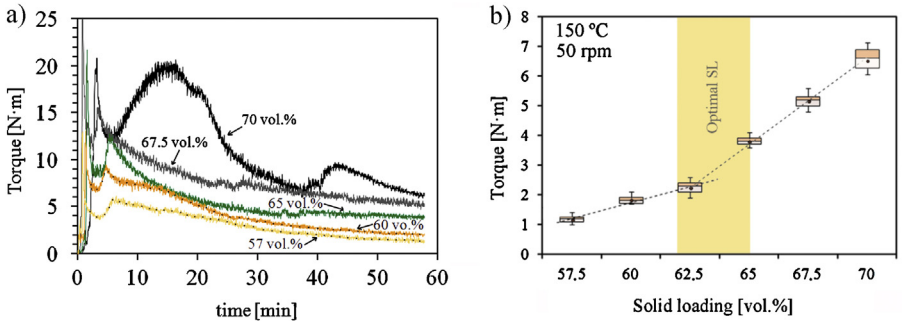

Fig. 2. (a) Mixing torque as a function of mixing time at 150 °C and 50 rpm for different powder volume content feedstocks and (b) mixing torque as a function of solid loading. The points represent the average torque values over 2 min (from minute 60 to minute 62) with values recorded each second. The upper and lower whiskers represent the maximum and minimum torque measured, respectively, the box represents the second and third quartiles, and the line represents the median.

Table 2
Binder composition.

Component	Acetyl*	Butyryl*	Hydroxyl*	Vol.%
CAB381-0.1	13	37	1.5	30
CAB551-0.01	2	53	1.5	10
PEG 20 k	–	–	–	58
PEG 10 k	–	–	–	2

* Percentage of side groups in chain.

with variable solid loadings ranging from 57.5 to 70 vol.% were prepared in a Haake Rheomex twin sigma rotor internal mixer, and the same mixing parameters were used for all feedstocks. The feedstocks were mixed at 150 °C and a rotor speed of 50 rpm for 1 h to ensure homogenisation. Capillary rheology measurements were conducted using a Rosand RH2000 capillary rheometer. The relationship between the length and the diameter of the capillary is 30/1 with capillary diameter of 1 mm. The density of the resulting solidified and pelletised feedstock was measured with a Micrometrics AccuPyc 1330 helium pycnometer. The feedstocks were employed to perform an entire μPIM process. A Battenfeld microinjection moulding machine was used to inject micro parts for tensile and bending tests. A vacuum atmosphere was used for both the thermal debinding and sintering stages. Solvent debinding in water at 60 °C for 2 h was carried out prior to thermal debinding. A Kammrath and Weiss micro-mechanical testing stage with a load cell of 1 kN was used to perform micro tensile tests at room temperature. Scanning electron microscopy (SEM) was performed using a Philips XL-30 microscope.

3. Results

3.1. Torque measurements

Monitoring the evolution of torque values with mixing time is conventionally used as a simple method to evaluate critical and optimal solid loadings. For example, in the work of Contreras et al. (2010) this technique, in combination with other methods, was employed to study the effect of different particle sizes and geometries. The torque versus mixing time curves of Invar 36 feedstocks with different solid loadings (Fig. 2(a)) exhibited two different behaviours after the mixing chamber was closed with all the components inside:

(i) An abrupt increase in the torque occurred followed by a gradual decrease until it stabilised. This behaviour was observed at solid loading below 67.5 vol.%
(ii) For 70 vol.%, an abrupt increase in torque occurred followed by a rapid decrease and a progressive increase thereafter. The torque values varied more erratically during this progressive increase. All these findings are considered evidence of critical solid loading. However, after reaching a maximum, the torque values decreased again and then stabilised.

This change in mixing behaviour is normally associated with solid loading near the critical powder volume content (CPVC), i.e., the minimum volume of binder necessary to completely embed powder particles.

As the powder content is increased, it becomes more difficult to incorporate powder into the binder and to achieve a homogeneous component distribution. If particle agglomeration occurs, mixing could also be hindered. Fig. 2(b) presents the average torque steady flow values after 60 min of mixing as a function of powder volume content. The box and whisker plots for each average value illus-trate the variability of the results during the last 2 min and thus of the homogeneity of the mixtures. A disruption in the torque versus solid loading dependence was observed at 62.5 vol.% feed-stock, as it can be seen from the change in the slopes of two straight lines fitting the experimental points. Vieira and Barreiros (2006) linked this fact with CPVC. However, they noted that for a better determination of the optimal solid loading the properties of sin-tered parts of compositions close to these points should be further evaluated.

In previous works, Hidalgo et al. (2012) have monitored a ceramic-type feedstock temperatures during mixing and have noted that the mixture temperature is higher than the programmed temperature for all feedstocks studied. This temperature difference became more intense as the solid loading increased and approxi-mately followed the torque behaviour. This behaviour was related to a particle friction effect and is in agreement with the princi-ple of torque measurements. Temperature and torque parameters are related to the energy necessary to displace and mix all compo-nents together. Greater friction between particles leads to a greater restriction to the feedstock flow, increasing the energy needed. In Cheremisinoff (1990) the totalised torque value (TTQ) calculated from torque rheology of different polymers is proposed as an use-ful parameter for several purposes. The energy employed during mixing can be summed up with TTQ, representing the area under the torque vs. time curve at a given time. This value, which repre-sents the necessary mixing energy during a given period of time, is also representative of the total energy dissipation rate in a sus-pension or in loaded polymeric blends. Abu-Orf and Örmeci (2004) used TTQ to estimate the relative network strength in suspensions. Escocio et al. (2011) evaluated the processability of polymer-filler composites with the TTQ parameter. In this work, TTQ is used to estimate of friction energy because binders are loaded in high concentrations and friction forces predominate over cohesion forces. The work energy supplied to the system by the rotors (E_t) represents a force (F) multiplied by a distance (d). In a torque rheometer, the distance covered by the blade is equal to the angular speed (N) expressed in rpm, multiplied by $2\pi r$, where the r is the aver-age blade radius. Considering that torque (M) is a function of force, $M = F \times r$, the work energy as a function of TTQ is given by the expression (1):

$$E_t = F \cdot d = 2 \cdot \pi \cdot r \cdot N \cdot \int_{t1}^{t2} \left(\frac{M(t)}{r} \right) \cdot dt = 2 \cdot \pi \cdot N \cdot TTQ \qquad (1)$$

Table 3
Torque rheology parameters after 60 min. From left to right, average torque values with standard deviation, temperature, totalised torque, energy supplied by the rotors, the specific energy for feedstocks with different solid loadings and the friction energy dissipated by heat.

Powder (vol.%)	$\bar{M} \pm SD$ (N m)	T (°C)	TTQ (J min)	E_t (kJ)	E_{sp} (J/g)	C_{feed}* (J/g °C)	E_{frict} (J/g)
57.5	1.17 ± 0.09	153.8	148.4	46.62	179.76	1.12	4.56
60	1.83 ± 0.11	154.9	190.2	59.75	222.99	1.08	5.29
62.5	2.24 ± 0.16	155.2	205.8	64.65	233.76	1.05	5.46
65	3.81 ± 0.12	155.9	247.7	77.82	275.88	1.01	5.96
67.5	5.17 ± 0.18	157.3	348.1	109.36	372.24	0.98	7.15
70	6.53 ± 0.27	159.1	469.3	147.43	487.54	0.94	8.55

* C_p calculated by the mixing rule considering $C_{Invar36}$ = 0.515 J/g °C, C_{CAB} = 1.55 J/g °C and C_{PEG} = 2.2 J/g °C.

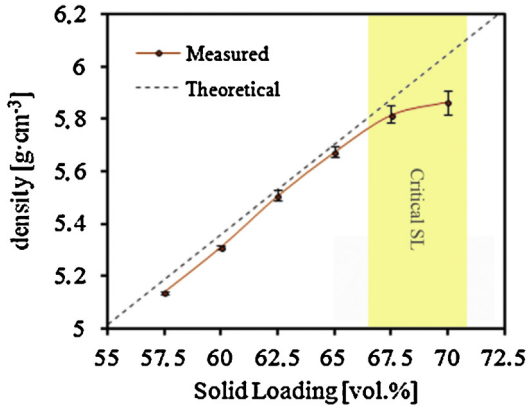

Fig. 3. Feedstock density as a function of solid loading measured with a helium pycnometer. Points (with corresponding error bars) represent the average values after four measurements in different portions of each pelletised feedstock batch. Dashed lines represent theoretical values as predicted with the mixing rule.

The specific energy of processing (E_{sp}) is obtained from E_t as a function of the material mass inside the mixing chamber (Eq. (2)),

$$E_{sp} = E_t \cdot m_{feed}^{-1}. \tag{2}$$

The percentage of specific energy in terms of heat dissipated by friction can be assessed considering the overheating of the feedstock (ΔT_{oh}) together with the specific heat (c_{feed}) of the feedstock,

$$E_{frict} = c_{feed} \cdot \Delta T_{oh} \tag{3}$$

Table 3 reports some of the mixing energy parameters assessed after 60 min along with the chamber temperatures. A progressive increase in the temperature and the energy necessary to mix feedstock's components was observed as the solid loading increased, with a remarkable increase between two consecutive solid loading values as the CPVC value was approached. This could be linked with the decreasing capacity of the binder system to lubricate all the powder particles as the solid loading increases, leading to an increase in the friction energy involved in the system which is dissipated as the temperature increases and also affects the torque values.

3.2. Density measurements

The CPVC was also determined with a density technique. For compositions above the critical solid loading, the amount of binder is insufficient to cover the particles and fill the remaining free volume. This results in the formation of voids inside the feedstock bulk; considering that no material is lost during the mixing process, this means that the density would be lower than the theoretical density calculated by the mixing rule. CPVC determination by measurement of the feedstock density takes this fact into account.

The density values of the different feedstocks are shown in Fig. 3. For all the different solid loadings up to 65 vol.%, the measured values were very close to the theoretical values. Nevertheless, all the values were lower than the corresponding theoretical values which can be explained by the occurrence of agglomerates. The deviation of the measured density values from the mean density calculated from four different portions of each batch was almost negligible in this range of solid loadings. From that point on, for 67.5 vol.% and 70 vol.% feedstocks, the marked divergence from the theoretical density indicates excess powder content, resulting in void formation. The variability of the results also indicates heterogeneities in the batch composition derived from a less efficient mixture, which may be attributed to the CPVC. These observations, taken together with the torque experimental results, suggest that the critical solid loading value should be placed at 67.5 vol.%, although the torque measurements do not provide clear evidences of the CPVC.

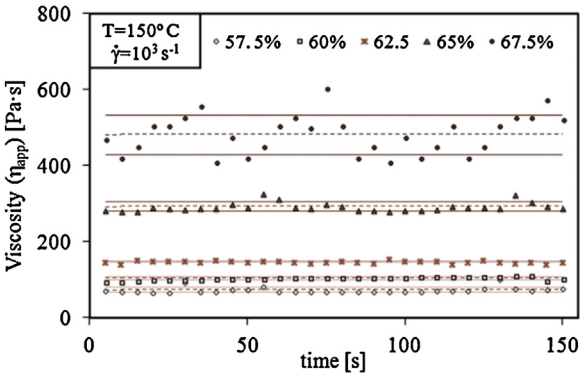

Fig. 4. Apparent viscosity values as a function of time for different powder volume content feedstocks tested at a shear rate of 1000 s^{-1} and 150 °C. Dashed lines represent the average value while straight lines enclose values within two standard deviations.

3.3. Capillary rheology

The homogeneity of the feedstocks was also evaluated by measuring the variability of the feedstock viscosity over time. This was accomplished using a capillary rheometer, which forced the melted feedstock to pass through a fine capillary. Hausnerova (2010) presented a very thorough work about capillary rheology in PIM. The feedstock viscosity, especially that of the highly charged PIM feedstocks, is sensitive to variations in composition. Although the torque rheometer also indicated heterogeneities, the capillary rheometer provides a more precise way to evaluate this characteristic. The torque rheometer evaluates the global feedstock's bulk at a given time, whereas the capillary rheometer measures finite portions of the feedstock's bulk. Fig. 4 shows apparent viscosity values as a function of time for different binder compositions at 150 °C and a shear rate of 1000 s^{-1}. Feedstocks up to 62.5 vol.% showed little variability in viscosity with time, with most values falling within the standard deviation interval. Slight heterogeneities were observed in the 65 vol.% feedstock, which maintains a highly constant viscosity over time, with some exceptions. Viscosity values became more erratic in the 67.5 vol.% feedstock, suggesting heterogeneity appropriate for the CPVC. Results could not be obtained at 70 vol.% because this feedstock exceeded the maximum viscosity detectable by the capillary rheometer under these conditions.

It is worth to note that this method could be sensitive to the experimental shear rates chosen. Hausnerova (2010) reported that viscosity values could be erratic at certain shear rates due to flow instabilities caused by other factors than the mentioned compositional heterogeneity, e.g. binder-powder segregations caused by shear. In Invar 36 feedstocks similar results were obtained after carrying out trials at 10 and 100 s^{-1}. Nevertheless, changes in the viscosity values with time for 67.5 vol.% under these conditions were smoother than those observed at 1000 s^{-1}. If other factors influencing severe flow instabilities at 1000 s^{-1} exist, they are likely driven by heterogeneities in the feedstock composition. This conclusion is supported by the heterogeneities observed after torque rheology and density measurements.

$$\log(\eta) = B + \frac{E_q}{R} \cdot \frac{1}{T} \tag{4}$$

Another sophisticated way to determine optimal and critical solid loading to support capillary rheometer measurements is by calculating the apparent flow activation energy (E_a) according to Eq. (4). Viscosity values are needed for at least three different

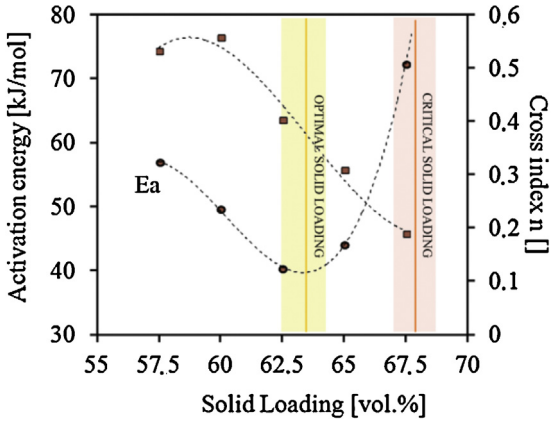

Fig. 5. Apparent flow activation energy and cross index m at 160 °C as a function of solid loading. Activation energy was calculated from viscosity values at 5000 s^{-1} at three temperatures (150 °C, 160 °C and 170 °C) according to the slope of the linear regression of the representation of the logarithm of viscosity versus the inverse of temperature.

temperatures with the rest of the conditions kept constant (shear rate, solid loading, etc.). Flow activation energy can be calculated from the slope of the logarithm of viscosity (η) versus the inverse of temperature (T), which should be a straight line. R is the gas constant and B is the logarithm of a reference viscosity at certain T. Viscosity values were measured at 150 °C, 160 °C and 170 °C and 5000 s^{-1}. The results are shown in Fig. 5, which plots the apparent flow activation energy as a function of solids loading. An increasing number of publications have reported the occurrence of a minimum in the flow activation energies and variations in other rheological parameters (such as the power law or Cross exponents) for solid loadings correlated with the optimal powder content. Contreras et al. (2010) registered this behaviour for feedstocks of superalloy powders with different particle sizes and particle distributions. Similar findings were reported by Kong et al. (2012) in stainless steel feedstocks and by Hidalgo et al. (2012) for a irregular shape ceramic powders feedstcoks. In the Invar 36 feedstock, a reduction of the Cross exponent occurred at 62.5 vol.% feedstock (Fig. 5), along with a minimum in the activation energy for this composition. Considering that result, the optimal solid loading for Invar 36 feedstocks could be between 62.5 vol.% and 65 vol.%. According to German and Bose (1997), the optimal solid loading should be around 5% less than the critical solid loading. This recommendation is based on the experience in PIM field. In the case of Invar 36 feedstocks the optimal solid loading seemed to occur at compositions around 67.5 vol.% which coincides with German's recommendation.

3.4. *μPIM of selected feedstocks*

A complete μPIM process was carried out for 57.5 vol.%, 60 vol.%, 65 vol.% and 67.5 vol.% feedstocks. Micro tensile and bending test specimens were injected in a Battenfeld microinjection moulding machine. The dimensions of the green parts as replicated from the mould are shown in Fig. 6(a). A nozzle temperature of 170 °C was selected and the mould was heated at 30 °C. Injection and post pressures of 1000–1200 bar and 500–600 bar (held during 5 s) respectively generally leaded to complete dense green parts without apparent flaws. The volume of dosage was also optimised. The presence of flaws as short shots, flash or warpage depended on the feedstock powder volume content thus injection conditions were varied around those values to minimise them.

Although 67.5 vol.% feedstocks were able to be injected, in some cases short shoots occurred at pressures near the maximum allowed by the injection machine. That demonstrates that this composition was almost at the limit, and that small differences in composition made the injection unfeasible. The weights of the apparently flawless injected micro-parts varied as shown in Fig. 6(b). Straight lines represent the average value while dashed lines represent the upper and lower standard deviations from the average values. The most variable results corresponded to 67.5 vol.%, although any pieces that were not completely injected were discarded for the analysis.

Fig. 7 shows the evolution of the mould filling during the injection optimisation process for a 60 vol.% feedstock and a 67.5 vol.% feedstock. The sequences were made varying the volume of dosage between 20 and 45 mm^3. Some differences were observed between the two processes. In the case of 60 vol.% feedstocks (Fig. 7(a)), the melted feedstock advanced evenly to fill the mould, expanding like a fan after reaching the end cavity of the part as it broadened after the tight channel. This behaviour could be linked with a viscoelastic fluid. However, the expansion after the broadening was not as evident in the 67.5 vol.% feedstock, and it seemed that the feedstock continued to move forward, retaining the shape of the tight channel like a typical plug flow. When this flow front reached the end of the part it was sent back and the end cavity was filled up with both a back flow and a forward flow, in this case from fresh melted feedstock coming through the tight channel. In a plug flow, the central part of the flow, enriched in powder particles, moves like a solid, while in the regions near the walls, the viscoelastic binder-rich feedstock facilitate the advance. A plug flow may form in CPVC situations because the binder system is

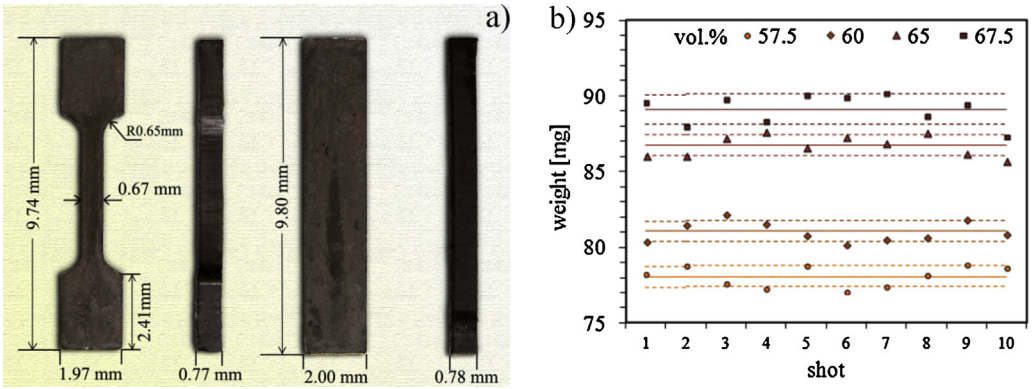

Fig. 6. (a) Green part dimensions as replicated from the mould cavity. The parts shown here correspond to 65 vol.% solid loading. (b) Variations in the weight of the apparently flawless injected micro-parts for different solid loading feedstocks. Straight lines represent the average value while dashed lines represent the upper and lower standard deviations from the average values.

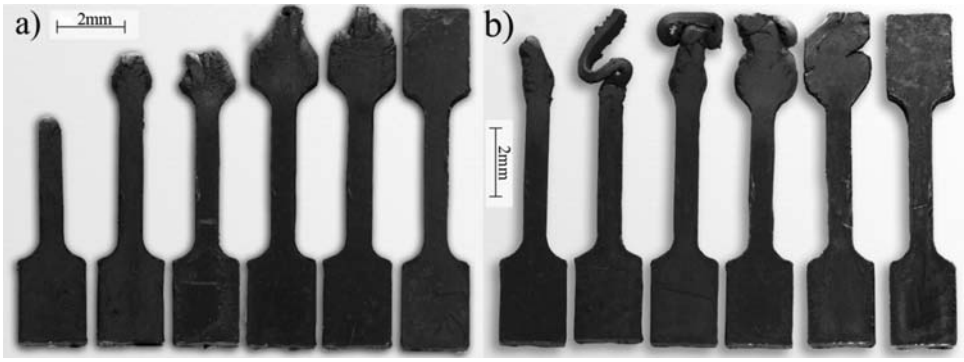

Fig. 7. Evolution of the mould filling during the injection optimisation process: (a) 60 vol.% feedstock and (b) 67.5 vol.% feedstock.

not able to lubricate powder particles and their movements are restricted. The pressure may also be responsible for the rejection of some of the binder from the core to the surface, worsening the effect of low binder content in the core.

Injection optimisation indicated that even though 67.5 vol.% solid loading showed signs of CPVC, it still had enough viscosity to be injected but also showed signs of undesirable plug flow. In that respect, 65 vol.% feedstocks showed good filling behaviour and good process reproducibility in terms of the micro part weight.

The occurrence of CPVC around 67.5 vol.% was also demonstrated by the analysis of SEM micrographs of the different compositions of injected micro parts shown in Fig. 8. In case of 57.5 vol.% and 60 vol.% micro parts (Fig. 8(a) and (b), respectively), low particle packing was observed with regions with high percentages of polymeric compounds indicating an excess of binder. Better packing of the powder particles was observed in 65 vol.% micro parts (Fig. 8(c)), with particles embedded more homogeneously in the binder system and without any regions with a high percentage of binder. At 67.5 vol.% solid loading (Fig. 8(d)), injected micro parts exhibited regions with a lack of binder surrounding powder particles, indicating that the critical solid loading was surpassed in some of the regions of the micro part.

3.5. Debinding optimisation

A two step binder removal process was carried out after injection. First, a solvent debinding step was performed in water to remove PEG and create an open channel to facilitate further thermal elimination of CAB without defect formation. Fig. 9 shows the evolution of the water solvent debinding over time for different solid loading feedstocks at 60 °C. In 3 h, 91.4 vol.% of PEG was removed, in the worst case corresponding to 57.5 vol.% micro parts. Unlike what would be commonly expected, a worsening of the extraction with solid loading due to higher packing of the particles, increasing solid loading positively affected binder removal. The best results were obtained with 65 vol.% and 67.5 vol.% parts, with almost 100% of the removable part eliminated after 3 h. There were no clear differences in the elimination rates. When solid loading is increased the particle packing commonly increases, reducing the possibility that PEG evacuates channels during debinding and hindering the diffusion from the core to the surface. This normally would lead to a reduced rate of elimination and less effective removal of the soluble part. Nevertheless, the thinness of the pieces and the small amount of removable part probably resulted in only slight differences. In the case of the 57.5 vol.% part, the effectiveness of the solvent debinding

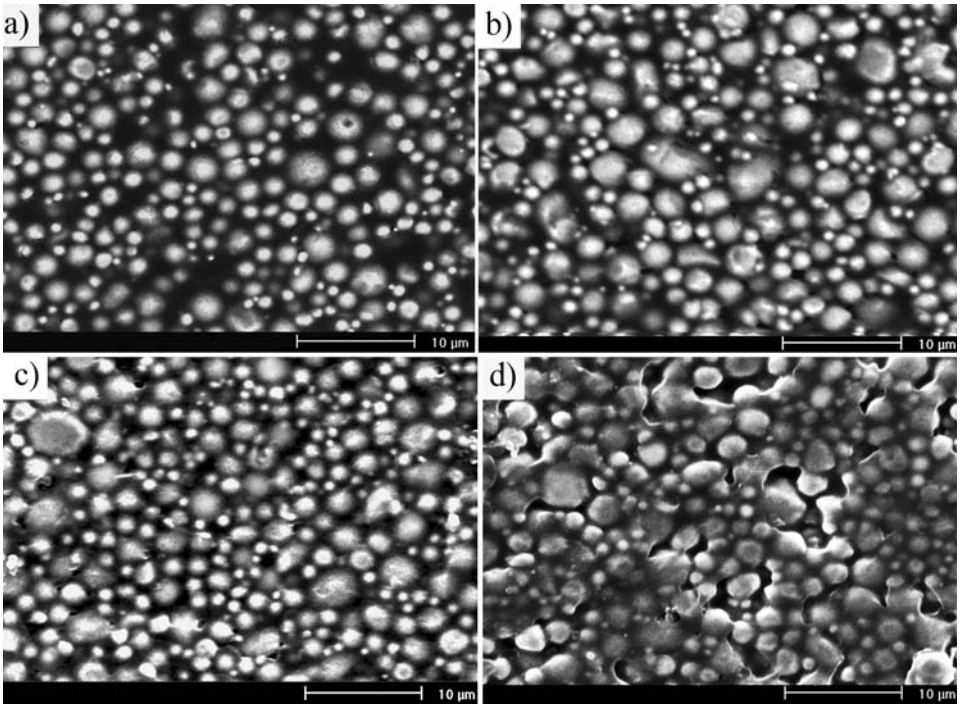

Fig. 8. Back scattering electron SEM images of the surfaces of injected parts: (a) 57.5 vol.%, (b) 60 vol.%, (c) 65 vol.%, and (d) 67.5 vol.%.

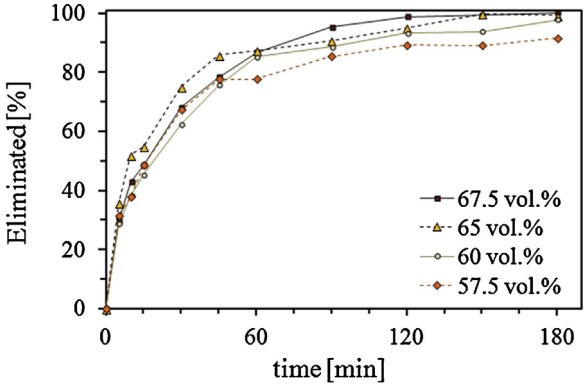

Fig. 9. Evolution of solvent debinding over time determined by measuring the removal of the soluble part at 60 °C using water as the solvent.

could be reduced because there is also more CAB. CAB has exhibited a good affinity with PEG, potentially causing some degree of miscibility between the two compounds. If this has occurred, CAB could retain some PEG, complicating its elimination. Another possible fact is a segregation of PEG and CAB due to the high shear force caused by the small diameters of the runners and micro parts. The shear force increases as the solid loading increases. Hence, PEG could migrate predominantly to the part surfaces, promoting the plug flow observed during injection of higher solid loading. The subsequent solvent extraction would be facilitated in such a case.

Thermal debinding in vacuum up to 500 °C for 1 h at a heating rate of 2 °C/min allowed for almost all of the remaining CAB to be burned out. Although a small percentage of organic compounds remained after thermal elimination, they presumably would be removed at higher temperatures by pyrolysis.

3.6. Sintering and micro-tensile tests

During the sintering stage, brown specimens were heated at several heating rates (2 °C/min or 5 °C/min) up to different temperatures (1000 °C or 1100 °C) in a vacuum atmosphere and held at the target temperature for 15 min. In Fig. 10(a), pieces after different stages of the PIM process are presented for the 57.5 vol.% feedstock heated at 2 °C/min to 1100 °C. The 57.5 vol.% parts had the largest contraction; hence the evolution of the parts' dimensions could be better observed. Due to the small size of the sintered parts, it was difficult to obtain reliable data on the densification of the parts by a helium pycnometry or by dilatometry. Therefore, the densification of the pieces was evaluated by direct measurements of the micro part dimensions and by investigating the microstructure. Fig. 10(b) shows the part shrinkage during the sintering process for different sintering conditions and solid loading compositions. Note that as the solid loading increased, the shrinkage decreased because less free volume was present after binder removal. This is a positive outcome when dealing with tolerances. The general tendency of the shrinkage indicated a better densification as the temperature and the heating rate were increased. In some cases, the shrinkage almost corresponded to the theoretically full densification of the parts, which could give a rough idea of the extent of densification.

Fig. 11 presents back scattering electron images of sintered 57.5 vol.% and 65 vol.% parts at 1100 °C and 5 °C/min. An apparently full austenite microstructure was developed at all compositions with similar grain sizes of around 50 μm in their longest diameter. Carbon content was measured with a LECO device resulting in no more than 0.06 mass%, and with highly consistent results for all solid loadings. Graphite precipitation was not observed, which is consistent with the results of Wittenauer (1996) which analysed Invar 36 compositions at these carbon contents. X-ray diffraction experiments confirmed the presence of typical Fe–36Ni austenite but also revealed a slight amount of ferrite formation that was not detected during microstructure inspection. The development of this austenitic microstructure suggests that the low CTE typical of Invar 36 alloys can be achieved.

Significant differences were observed in the pore quantity and the pore net distribution. In the case of 57.5 vol.% (Fig. 11(a)), the pore density was high and heterogeneous with small pores in the range of the particle size or below, but large areas of bigger pores were also observed and were sometimes interconnected, forming clusters. In contrast, the 65 vol.% (Fig. 11(b)) parts exhibited less large pores than the 57 vol.% parts, they were more homogeneously distributed and no interconnected pore cluster areas were observed. These differences could be linked with the shrinkage results, giving an idea of the part densification. However, a similar quantity of small pores could be associated with residual porosity after the sintering of small particles. Large pores may occur because of the low packing of powder particles and voids left by binder removal that could not be densified and closed by mass diffusion during sintering. After the sintering cycle, original particles and particle sintering necks were still observed in both the 57.5 vol.% and 65 vol.% microstructures. For all powder contents except 57.5 vol.%, a fine oxide layer was detected surrounding some ancient particles. In some cases, this layer was discontinuous and sintering necks were formed. Although a carbo-reductive process was expected between possible oxide layers and the residual organic binder after thermal degradation, differences in the internal pressures and CO/CO_2 ratios due to closer arrangement of particles may lead to differences in the effectiveness of oxide reduction or oxidation due to CO_2 during the sintering cycle.

Finally, micro parts sintered under the optimal conditions (1100 °C and 5 °C/min) were subjected to micro-tensile experiments. Zhao et al. (2009) discussed the limitations and issues in correctly interpreting micro tensile experiments. This work

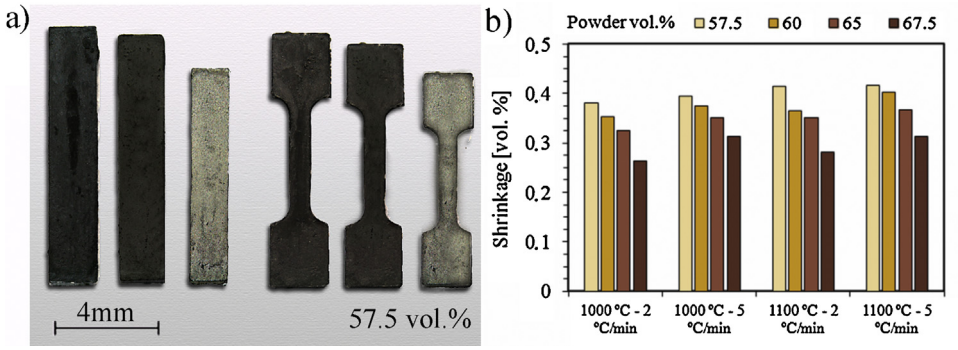

Fig. 10. (a) Examples of the variation in part dimensions during different stages of the μPIM process for the 57.5 vol.% feedstock. From left to right for each part geometry: green part, brown part after debinding and sintered part. (b) Shrinkage of the sintered part at different sintering conditions and solid loadings.

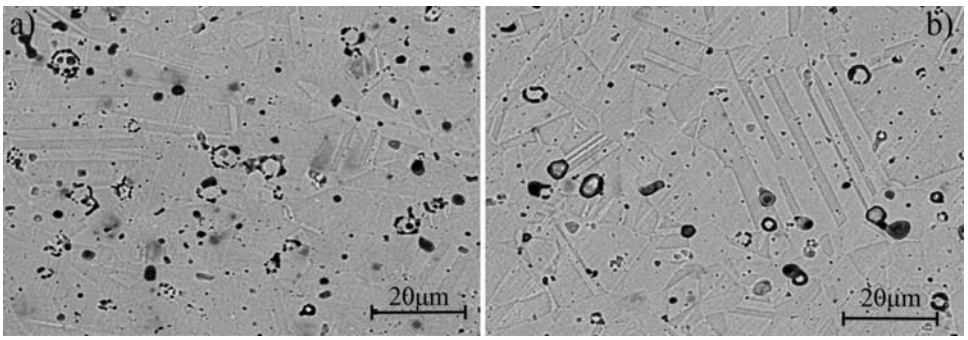

Fig. 11. Back scattering electron SEM images for sintered micro parts at 1100 °C and 5 °C/min: (a) 57.5 vol.% and (b) 65 vol.%.

Table 4
Different mechanical properties derived from engineering stress and strain curves for different solid loading sintered micro parts.

Solid loading (vol.%)	57.5	60	65	67.5
Tensile strength (MPa)	478 ± 20	499 ± 28	510 ± 23	471 ± 25
Yield strength (0.2% offset) (MPa)	248 ± 21	262 ± 20	280 ± 19	255 ± 23
Young's modulus (GPa)	57 ± 1	57 ± 1	52 ± 3	57 ± 1
Elongation (%)	30 ± 3	26 ± 2	27 ± 2	25 ± 3

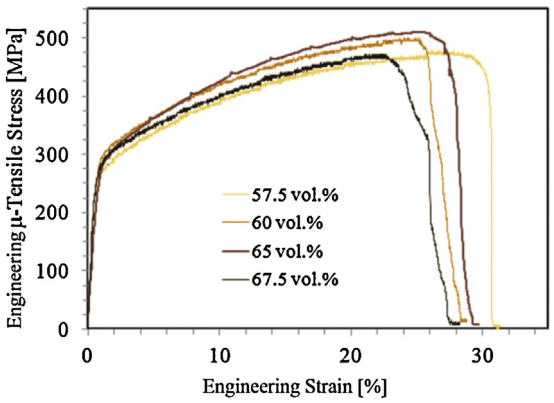

Fig. 12. Engineering stress and strain curves for sintered tensile micro parts with different solid loadings.

assumes errors in strain measurements as the data were collected directly from the cross head displacement without any extensometers, digital image correlation or laser interferometry. Thus, only engineering results are presented here. However, as the tests were performed on the same device, the results are valid for comparative purposes. Fig. 12 shows stress and strain engineering curves for different solid loading sintered micro parts, and Table 4 collects some mechanical properties derived from these curves. The ASTM designation A658 covers 36 percent nickel-iron alloy and specifies a tensile strength of 448–552 MPa, a minimum yield strength (0.2% offset) of 241 MPa and a minimum elongation of 30% for a wrought material. The results derived from the micro-tests were consistent with these specifications despite the parts were fabricated by powder metallurgy. The value of Young's modulus (E) was similar regardless of solid loading with the exception of 65 vol%. The values of the offset yield strength and tensile strength varied with the solid loading, increasing with higher solid loading up to a maximum of 65 vol.%. This fact could be most likely correlated with the dependence of porosity on solid loading. As the porosity increases, less effective area is available to withstand applied forces. Furthermore, pores could act as stress concentrators. However, despite the fact that elongation values are not completely reliable, better elongation results were obtained at 57.5 vol.%, with the greatest area fraction of voids and the lowest spatial separation between voids. Desrpés (2005) analysed the factors influencing the ductile behaviour of porous nickel-based superalloys to perform simulations on the mechanical behaviour of these alloys. The result obtained with 57.5 vol.% Invar 36 feedstock, may contradict predictions of the most probable void coalescence, and thus most probable catastrophic failure, of materials with high porosity contents. Other factors could affect ductility such as the extent of dislocation generated after sintering. Nevertheless, a coherent explanation may be developed based on the fact that in the 57.5 vol.% micro part, there were not appreciable oxide layer embedding original particles. This fine oxide layer was observed at all other compositions, explaining the poorer elongational results of those samples. In the case of the 67.5 vol.% parts, the diminution of mechanical properties could be presumably explained by a deterioration of the green part characteristics due to a less effective injection. Although these parts contained less porosity and better microstructural features, macro defects arose in these parts.

Carefully taking into account the micro mechanical test results, the mechanical behaviour at different solid loadings indicated an optimal solid loading of around 65 vol.%. This would confirm all the results for solid loading optimisation. These parts exhibited good particle packing, leading to better tolerances and mechanical properties without the macro defects that arise at 67.5 vol.%.

4. Conclusions

This work combined several techniques to determine the critical powder volume content of Invar 36 feedstocks based on a CAB and PEG binder system. This type of feedstock was formulated and tested to carry out an entire µPIM process. The following conclusions were drawn:

- All the used techniques combined with the microinjection results and micro mechanical tests pointed to an optimal solid loading of 65 vol.%.
- The 67.5 vol.% feedstock still flows sufficiently well to be injected, but it was at the limit of the CPVC value; it presented compositional heterogeneities and other indications of proximity to the CPVC such as a deviation from the theoretical density value.
- The proposed binder system generally results in good flow behaviour and technical characteristics of the feedstock and sintered parts, enabling its use in µPIM of an Invar 36 alloy.

Acknowledgments

The authors wish to thank GUZMÁN GLOBAL S.L. and MIMTECH ALFA for their collaboration on the ECOPIM project (Ref. IPT-2011-0931-20000) that was funded by the Spanish Ministry of the Economy and Competitiveness. Furthermore, the authors would like to acknowledge the strong support from the ESTRUMAT projects (Ref. S2009/MAT-1585), which were funded by the CAM-Consejería Educación Dir. Gral. Universidades e Investigación, and from the COMETAS project (Ref. MAT2009/14448-C02-02), which was funded by the Spanish Ministry of the Economy and Competitiveness.

References

Abu-Orf, M., Örmeci, B., 2004. A New Tool for Measuring Biosolids Floc Strength. IWA Publishing, USA.

Attia, U.M., Alcock, J.R., 2011. A review of micro-powder injection moulding as a microfabrication technique. Journal of Micromechanics and Microengineering 21.

Bernardo, E., Hidalgo, J., Jimenez-Morales, A., Torralba, J.M., 2012. Feedstock development for powder injection moulding of zirconium silicate. Powder Injection Moulding International 6, 4.

Bitkulov, I.K., Burkhanov, A.M., Kazantsev, V.A., Mulyukov, R.R., Mulyukov, K.Y., Safarov, I.M., 2006. Effect of severe plastic deformation on the properties of the Fe–36% Ni invar alloy. Physics of Metals and Metallography 102, 91–96.

Contreras, J.M., Jimenez-Morales, A., Torralba, J.M., 2010. Experimental and theoretical methods for optimal solids loading calculation in MIM feedstocks fabricated from powders with different particle characteristics. Powder Metallurgy 53, 34–40.

Cheremisinoff, N., 1990. Product Design and Testing of Polymeric Materials. Marcel Dekker, USA.

Chi, Z., Jing, L., Rong, X., 2011. An investigation on a new type of Fe–Ni alloy in MIM process. Advanced Materials Research 311–313, 653–656.

Desrpés, M., 2005. On the Evaluation of Ductile Behaviour of Porous Nickel-Based Superalloys Using Finite Element Method Department of Mechanical Engineering. McGill University, Montreal.

do Nascimento, R.M., Buschinelli, A.J.A., Klein, A.N., Martinelli, A.E., 2006. Microstructure and dilatometric behavior of powder injection molded low-expansion alloys. International Journal of Powder Metallurgy 42, 29–38.

Escocio, V.A., Visconte, L.L.Y., de Carvalho, M.B.M., Nunes, R.C.R., Altstaedt, V., 2011. Thermal and dynamic mechanical characterization of TPU/Mica composites prepared by torque rheometer. Polimeros-Ciencia E Tecnologia 21, 240–245.

German, R.M., Bose, A., 1997. Injection Molding of Metals and Ceramics. Metal Powders Industry Federation.

Hatate, M., Sumimoto, H., Nakamura, K., 1990. Influence of carbon and nickel on linear thermal-expansion coefficient in low thermal-expansion Fe–Ni–C alloys. Journal of the Japan Institute of Metals 54, 1036–1040.

Hausnerova, B., 2010. Rheological characterization of powder injection molding compounds. Polimery 55, 3–11.

Heaney, D.F., 2012. Handbook of metal injection molding. Woodhead Publishing in Materials.

Hidalgo, J., Jimenez-Morales, A., Torralba, J.M., 2012. Torque rheology of zircon feedstocks for powder injection moulding. Journal of the European Ceramic Society 32, 4063–4072.

Hidalgo, J., Jimenez-Morales, A., Torralba, J.M., 2013. Thermal stability and degradation kinetics of feedstocks for powder injection moulding – a new way to determine optimal solid loading? Polymer Degradation and Stability 98, 8.

Khomenko, O.A., 2007. Origin and specific features of invar anomalies of physical properties: Fe–Ni alloys with an FCC lattice. Physics of Metals and Metallography 104, 146–156.

Kong, X., Barriere, T., Gelin, J.C., 2012. Determination of critical and optimal powder loadings for 316L fine stainless steel feedstocks for micro-powder injection molding. Journal of Materials Processing Technology 212, 2173–2182.

Maslyuk, V.A., Panasyuk, O.A., Vlasova, O.V., 2003. Physical, technological and magnetic properties of powder iron–nickel alloys. Powder Metallurgy and Metal Ceramics 42, 536–539.

Minseok, S., Min Soo, P., Jin Kon, K., Il Bum, C., Kyung Ho, K., Hwan Jin, S., Sangho, A., 2005. Water-soluble binder with high flexural modulus for powder injection molding. Journal of Materials Science 40, 1105–1109.

Nadutov, V.M., Kosintsev, S.G., Svystunov, E.O., Zaporozhets, O.I., 2009. Interatomic interaction and magnetostriction in Invar Fe–Ni–C-Based Alloys. Metallofizika I Noveishie Tekhnologii 31, 1021–1034.

Nadutov, V.M., Kosintsev, S.G., Svystunov, Y.O., Tatarenko, V.A., Yefimova, T.V.,
2006. Magnetic properties of alloyed invar alloys on the base of Fe–Ni–C. Metallofizika I Noveishie Tekhnologii 28, 39–48.

Rajabi, J., Muhamad, N., Sulong, A.B., 2012. Effect of nano-sized powders on powder injection molding: a review. Microsystem Technologies-Micro-and Nanosystems-Information Storage and Processing Systems 18 (12), 1941–1961.

Ruh, A., Piotter, V., Plewa, K., Ritzhaupt-Kleissl, H.-J., Hausselt, J., 2012. Studies on size accuracy of microgear wheels produced by powder injection molding of zirconia feedstocks. International Journal of Advanced Manufacturing Technology 58, 1051–1059.

Suri, P., German, R.M., de Souza, J.P., 2009. Influence of mixing and effect of agglomerates on the green and sintered properties of 97W–2.1Ni–0.9Fe heavy alloys. International Journal of Refractory Metals and Hard Materials 27, 683–687. Vieira, M.T., Barreiros, F.M., 2006. PIM of non-conventional particles. Ceramics International 32, 297–302.

Wittenauer, J., Yaney, D.L., Lewis, R.E., 1994. Microyielding in Fe–36Ni: role of carbon and thermal processing. Scripta Metallurgica Et Materialia 31, 1531–1536.

Wittenauer, J., 1996. Factors affecting the mechanical strength of Fe–36Ni Invar. Proceedings of the "Invar Effect: A Centennial Symposium" Conference, 231–238.

Zhao, Y.H., Guo, Y.Z., Wei, Q., Topping, T.D., Dangelewicz, A.M., Zhu, Y.T., Langdon, T.G., Lavernia, E.J., 2009. Influence of specimen dimensions and strain measurement methods on tensile stress-strain curves. Materials Science and Engineering: A-Structural Materials: Properties Microstructure and Processing 525, 68–77.